Aerotecnica Missili & Spazio
https://doi.org/10.1007/s42496-022-00137-2

ORIGINAL ARTICLE

Autonomous Wheel Off-Loading Strategies for Deep-Space CubeSats

Andrea Pizzetti[1] · **Antonio Rizza**[1] · **Francesco Topputo**[1]

Received: 28 June 2022 / Revised: 12 September 2022 / Accepted: 14 September 2022

Abstract

Deep-space CubeSats missions require careful trade-offs on design drivers such as mass, volume, and cost, while ensuring autonomous operations. This work elaborates the possibility of off-loading the reaction wheels without the need of carrying a bulky and expensive reaction control system or the field-dependent magnetotorquers. The momentum accumulated along two body axes can be removed by either offsetting the main thruster with a gimbal mechanism or by tilting differentially the solar wings. The dumping on the third axis can be still accomplished by imposing a specific attitude trajectory with the motion of either the gimbal or the arrays drive mechanism. The M-Argo CubeSat is selected as case study to test the techniques along its deep-space trajectory. The strategies decision-making is autonomously carried out by a state machine. The off-loading during the cruising arcs employs the gimballed thruster and takes typically 3 h, granting a mass savings of more than 99% with respect to the usage of a reaction control system. The trajectory is shown to have negligible differences with respect to the nominal one, since the thrust is corrected accordingly. During the coasting arcs, the solar arrays are tilted and several hours are required, depending on the Sun direction and intensity, but the propellant is completely saved. Sensitivity analyses are also carried out on the initial angular momentum components and the center of mass displacement to check the robustness of the algorithms.

Keywords Reaction wheel · Off-loading · Desaturation · Deep space · CubeSat · M-Argo

1 Introduction

In the last years, the space sector has been characterized by a strong push in the nano-satellite class, enabling possibilities of exploration and technological demonstrations at relatively low costs. When they were first designed, CubeSats were addressed to Low Earth Orbits (LEO) missions, mainly for educational purposes. Now they are planned to be used by national space agencies also for interplanetary missions, with a high scientific return. Following the success of MarCO [1], several deep-space CubeSats missions have been scheduled, such as NEA Scout, Lunar IceCube, Lumio, Juventas & Milani and M-Argo [2–5].

All of these platforms use Reaction Wheels (RWs) to reject the attitude disturbances and control the orientation. These actuators are highly reactive and precise; however, when one wheel reaches the maximum angular rate, it is said to be *saturated* and can not produce torques anymore. If this occurs, the angular momentum must be removed from the wheel, reducing its speed while providing an opposite torque on the Spacecraft (S/C) to avoid drifts of the attitude. Such procedure is known as desaturation or Wheel Off-Loading (WOL).

This article outlines the development and feasibility of novel autonomous WOL strategies. These techniques will not require the use of any dedicated momentum-management device that is usually carried on-board, like a Reaction Control System (RCS) or a set of Magnetotorquers. Instead, they will exploit components typically devoted to other duties: the propulsion system, if coupled with a pointing mechanism, and the Solar Arrays (SAs), if they can be differently tilted by a Solar Array Drive Mechanism (SADM).

To work properly, RCS and Magnetotorquers require respectively the presence of additional propellant and magnetic field. These are not resources easily available in deep-space missions, where the satellite has heavy constraints in terms of mass and spends most of its lifetime in heliocentric

A. Rizza and F. Topputo: Thesis Advisor.

✉ Andrea Pizzetti
andrea1.pizzetti@mail.polimi.it

[1] Department of Aerospace Science and Technology, Politecnico di Milano, Via La Masa 34, 20156 Milan, Italy

orbits far from the magnetic influence of the planets. Instead, employing the same thruster that is used for the orbital cruising also for desaturation allows to keep on-board only the main propellant tank and save mass thanks to the inherent higher efficiency of thrusters with respect to RCS. Furthermore, strategies based on SAs require solar illumination, which is typically always achieved in interplanetary missions.

The techniques will be therefore demonstrated using a deep-space mission as a case study. The choice has fallen on the Miniaturised Asteroid Remote Geophysical Observer (M-Argo), a 12U CubeSat aiming to rendezvous with a Near-Earth Asteroid (NEA) after an autonomous deep-space travel [6]. The satellite is characterized by an assembly of 4 RWs, a gimballed ion thruster, and two large SAs. It is therefore the perfect candidate to prove these techniques. Moreover, since the CubeSat platforms are very good technology demonstrators and they experienced exponential success in the last years, it is natural to consider this class of satellites, in view of a future in-orbit demonstration.

Two different families of WOL strategies have been developed, depending on the scenario where they can be applied:

- **Cruising Arc**. During cruising, the thruster is active and produces a reference force F_{ref} along a pre-defined pointing vector $\hat{\boldsymbol{\alpha}}$. By making use of a gimbal mechanism and offsetting the thrust vector, it should be possible to generate desaturation torques about specific directions. In this case, the challenge is to not affect the reference trajectory with spurious forces, while still having the same level of thrust along $\hat{\boldsymbol{\alpha}}$.
- **Coasting Arc**. During the coasting arcs, the power drawn from the thruster is not present, and therefore there is no need to have both SAs facing the Sun continuously. By rotating them in a differential way, it could be possible to produce torques due to Solar Radiation Pressure (SRP) differences between the two.

The article is structured as follows. In Sect. 2, M-Argo is analyzed for what regards its mission objectives, operations, and system architecture. In Sect. 3, the techniques are outlined and linked together through the usage of a State Machine (SM). In Sect. 4, the results of the simulations and sensitivity analysis will be presented. Concluding remarks are given in Sect. 5.

2 Case Study

The M-Argo CubeSat will be released in a parking orbit around the Sun-Earth L2 point. A NEA target screening has been carried out during the mission analysis phase to identify the envelop of the most promising reachable asteroids [7]. In this article, the fuel-optimal trajectory to reach asteroid 2010-UE51 will be considered. Its thrust profile, reported in Fig. 1, is characterized by *thrust bins*. Each bin corresponds to a 1-week activity segment, composed of a cruising arc of 6 days and a coasting arc of 1 day, during which the thruster is switched on and off respectively [6].

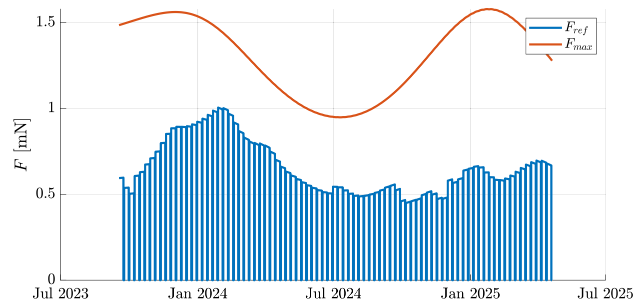

Fig. 1 Reference and maximum thrust during the fuel-optimal trajectory

The time period considered in the simulations will be 4–11 February 2024 because the correspondent thrust bin is associated with the worst-case scenario. In fact, in that cruising arc there is the lowest difference between the reference thrust level and the maximum one, i.e. the least capability of exceeding the reference value.

For what concerns the S/C, its properties are reported in Table 1, while the packed and deployed configurations are displayed in Fig. 2. M-Argo is characterized by two large SAs, each one with 4 6U-XL Solar Panels (SPs). The absorption, specular and diffusive coefficients considered are the ones associated with anodized aluminum for the body faces and last-generation solar cells for the SPs [8].

The CubeSat encompasses 4 RWs in a pyramid configuration along -x and a set of 12 RCs distributed in triads in the corners. The actuators data is reported in Table 2.

The propulsion system is a gridded ion engine with a gimbal mechanism that provides excursions up to 15°. As the propulsion is electric, the maximum thrust level and specific impulse are computed through polynomial fitting from the input power, which is in turn retrieved from the S/C distance from the Sun [7]. The typical specific impulse is on the order of ≈ 3500 s.

3 WOL Strategies

For the context of this work, three reference frames are identified in Fig. 3. Other than the inertial frame XYZ, denoted with n, and the body frame xyz, denoted with b, the pointing frame $\delta\beta\alpha$, denoted with p, is also defined.

Table 1 Physical and optical properties of M-Argo body, solar panels and solar arrays

Body[1]		SP[2]		SA			Body	SP
a	0.25 m	h_{SP}	0.209 m	h	0.209 m	ρ_s	0.8	0.0727
b	0.25 m	l_{SP}	0.3265 m	l	1.306 m	ρ_d	0.08	0.007
c	0.366 m	m_{SP}	0.453 kg	m_{SA}	1.812 kg			
m_{tot}	27.5 kg							

[1] 5th ESA CubeSat Industry Days.

[2] GomSpace NanoPower MSP Datasheet

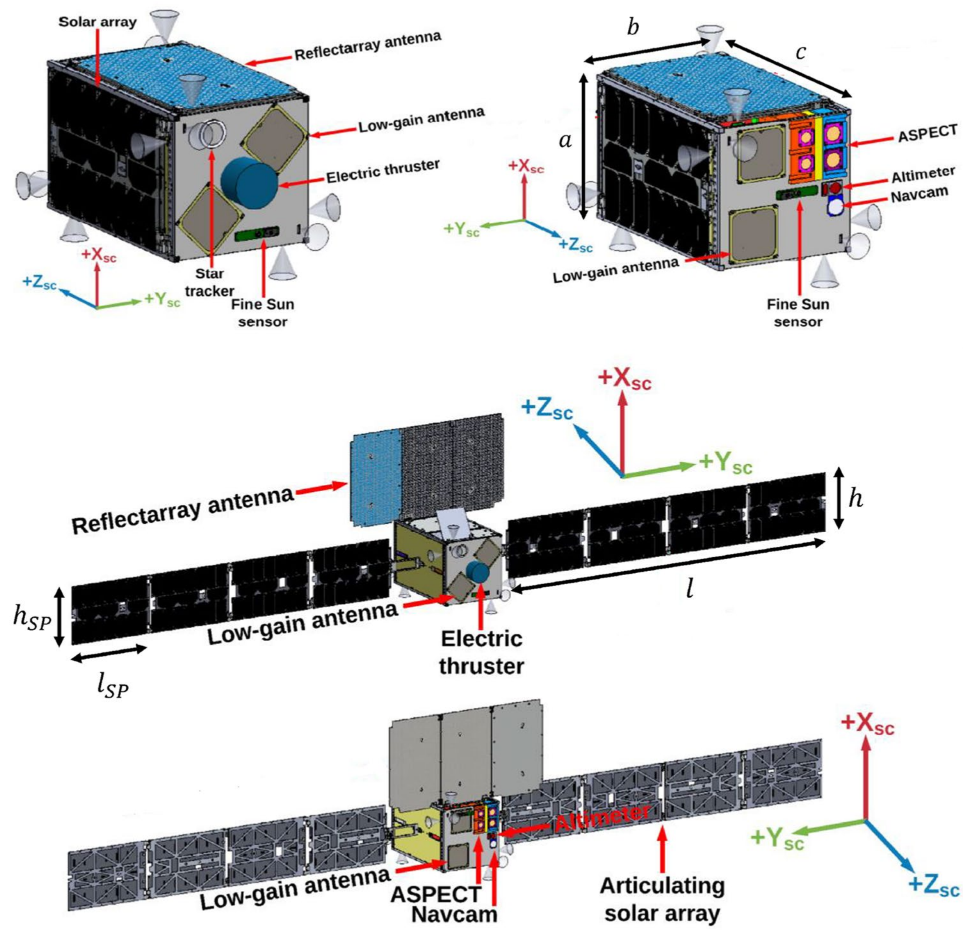

Fig. 2 M-Argo in packed and deployed configuration (5th ESA CubeSat Industry Days)

Table 2 Data of M-Argo actuators

RWS[1]		RCS[1]	
T_{max}	2 mNm	F_{max}	1 mN
h_{max}	19 mNms	I_{sp}	16 s

Attitude is expressed in terms of Direction Cosines Matrix (dcm) and follows the convention in (1), where the subscript refers to the frame in which the vector $\boldsymbol{x}$ is expressed.

$$\boldsymbol{x}_b = A_{b/p}\boldsymbol{x}_p = A_{b/p}A_{p/n}\boldsymbol{x}_n = A_{b/n}\boldsymbol{x}_n. \tag{1}$$

The p frame is slowly rotating with respect to n, according to the dynamics of the pointing vector $\hat{\boldsymbol{\alpha}}$ and of the Sun direction $\hat{\boldsymbol{S}}$ along the trajectory. Its orientation is given by (2).

$$A_{p/n} = \begin{bmatrix}\delta & \beta & \alpha\end{bmatrix}^T \qquad \begin{aligned} \alpha &= \hat{\boldsymbol{\alpha}}_n \\ \beta &= \hat{\boldsymbol{\alpha}}_n \wedge \hat{\boldsymbol{S}}_n \\ \delta &= \beta \wedge \hat{\boldsymbol{\alpha}}_n. \end{aligned} \tag{2}$$

During normal cruising, b is ideally coincident with p, because the z-axis is pointed along $\hat{\boldsymbol{\alpha}}$ and the y-axis is aligned perpendicularly to $\hat{\boldsymbol{S}}$ to maximize the power income. The desired body attitude would then be given by $A_{p/n}$. However, during WOL strategies that involve an attitude motion,

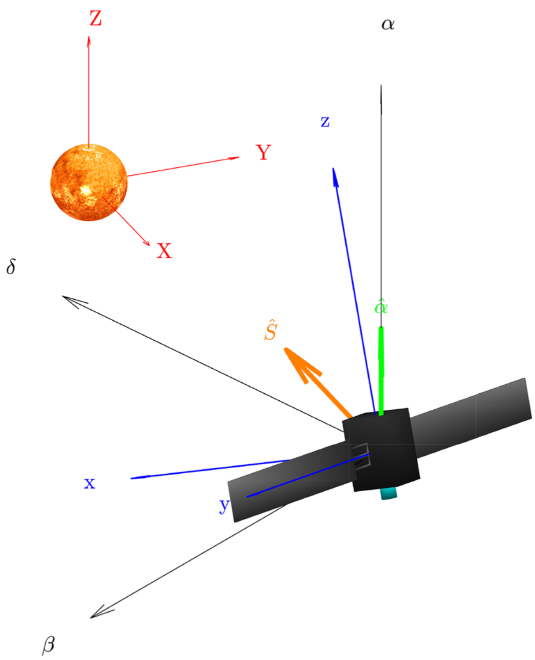

Fig. 3 Inertial, pointing and body frames

the two frames could become misaligned. In these cases, since $A_{p/n}$ is known, it is convenient to express the attitude guidance trajectories with respect to p, using just $A_{b/p}$.

3.1 Cruising

The WOL cruising strategies involve the use of the gimbal mechanism of the thruster to produce torques by off-setting the thrust vector from the Center Of Mass (COM) direction.

Referring to Fig. 4, the gimballed thrust direction $\hat{\boldsymbol{g}}$ can be expressed in terms of the excursion angles θ_1 and θ_2 about the y-axis and x-axis respectively.

As shown in Fig. 5, $A_{b/p}$ can be instead expressed in terms of the attitude angles ϕ_1 and ϕ_2, which represents the slewing around the β-axis and δ-axis respectively.

During cruising, M-Argo is nominally subjected to a reference thrust force F_{ref} aligned along $\hat{\boldsymbol{\alpha}}$. If the gimbal mechanism is used, the direction of the thrust changes to $\hat{\boldsymbol{g}}$ and the thrust must eventually increase to a new level $F_{com} > F_{ref}$ to still have the same intensity along the pointing vector. In other words, the projection of the commanded thrust vector $\boldsymbol{F}_{com}$ along $\hat{\boldsymbol{\alpha}}$ must be equal to F_{ref}. This condition is imposed to obtain the commanded throttle law in (3).

$$
\begin{aligned}
&\boldsymbol{F}_{ref} = F_{ref}\,\hat{\boldsymbol{\alpha}}_n \\
&\boldsymbol{F}_{com} = F_{com}\,\hat{\boldsymbol{g}}_n = F_{com}\left(A_{n/b}\,\hat{\boldsymbol{g}}_b\right) \\
&\boldsymbol{F}_{com} \cdot \hat{\boldsymbol{\alpha}}_n \equiv F_{ref} \;\rightarrow\; F_{com} = \frac{F_{ref}}{\left(A_{n/b}\,\hat{\boldsymbol{g}}_b\right) \cdot \hat{\boldsymbol{\alpha}}_n}
\end{aligned}
\tag{3}
$$

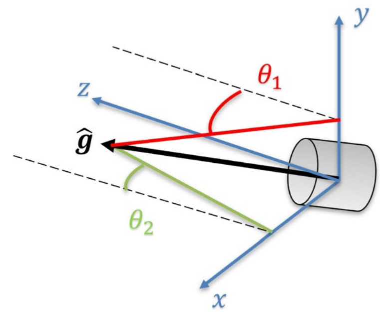

$$
\hat{\boldsymbol{g}}_b = \begin{bmatrix} \sin\theta_1 \\ \sin\theta_2 \\ \sqrt{1-(\sin\theta_1)^2-(\sin\theta_2)^2} \end{bmatrix}
$$

Fig. 4 Mapping of the gimballed thrust direction

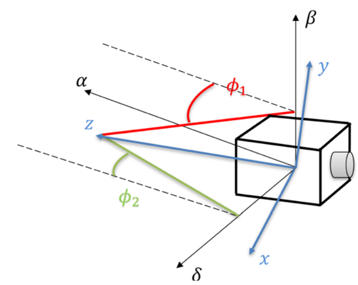

$$
A_{b/p} = \begin{bmatrix} \cos\phi_1 & 0 & -\sin\phi_1 \\ 0 & \cos\phi_2 & -\sin\phi_2 \\ \sin\phi_1 & \sin\phi_2 & \sqrt{1-(\sin\phi_1)^2-(\sin\phi_2)^2} \end{bmatrix}
$$

Fig. 5 Mapping of the attitude during cruising

3.1.1 Gimbal Strategy

This strategy dumps the momentum accumulated on the x and y axes, maintaining a fixed attitude. As shown in (4), the torque components in body frame are directly proportional to the sine of the gimbal angles, assuming the COM perfectly aligned along z. This assumption will be later relaxed in Subsect. 4.3.

$$
\boldsymbol{T} = \begin{bmatrix} 0 \\ 0 \\ -\frac{c}{2} \end{bmatrix} \times F_{com}\,\hat{\boldsymbol{g}}_b = F_{com}\begin{bmatrix} \frac{c}{2}\sin\theta_2 \\ -\frac{c}{2}\sin\theta_1 \\ 0 \end{bmatrix}
\tag{4}
$$

The higher the torque, the larger the value of momentum that can be off-loaded. Therefore, the ratio of the angular momentum components can be approximated to the ratio of the torques required to dump them. In this way, if one angle is fixed and the other is computed inverting (5), the two momentum components can be dumped at the same time.

$$\frac{h_y}{h_x} \approx \frac{T_y}{T_x} = \frac{-\frac{c}{2}\sin\theta_1}{\frac{c}{2}\sin\theta_2} = -\frac{\sin\theta_1}{\sin\theta_2} \tag{5}$$

The angle that is first imposed is the one associated with the highest angular momentum and is set equal to a pre-selected maximum value of $\theta_{max} = 5°$. Depending on the signs of the momentum components, all the cases can be covered using (6).

$$\begin{aligned} &|h_x| > |h_y| \rightarrow \begin{cases} \theta_2 = -\theta_{max}\mathrm{sgn}(h_x) \\ \theta_1 = \arcsin\left(-\frac{h_y}{h_x}\sin\theta_2\right) \end{cases} \\ &|h_x| < |h_y| \rightarrow \begin{cases} \theta_1 = \theta_{max}\mathrm{sgn}(h_y) \\ \theta_2 = \arcsin\left(-\frac{h_x}{h_y}\sin\theta_1\right) \end{cases} \end{aligned} \tag{6}$$

3.1.2 BETA Strategy

As shown in (4), only torques perpendicular to the thruster axis can be produced by making use of the gimbal. However, this does not imply that the momentum accumulated on z can not be off-loaded.

This has been partially addressed using the *natural* movement of this axis in specific orbits, such as geostationary [9] or lunar transfer orbits [10]. A complete rotation of the body thruster axis generally occurs in one day for the former and in less than one month for the latter cases. Since the angular momentum is fixed inertially in the axis in which it was originally generated, after sufficient movement along the trajectory the thruster axis becomes orthogonal to the momentum, which can be off-loaded by making use of the Gimbal strategy. However, to use this approach in deep space missions, with orbital periods around the Sun measured in years, RWs of high capacity are required and therefore not practical, especially in the case of CubeSats.

Alternatively, one could think to use a series of consecutive mirror maneuvers, performed by both slewing the S/C and rotating the gimbal of 90° [11]. In this case, unfortunately, the gimbal must have a large excursion range and the propellant is completely wasted since the thrust is not directed in the desired direction.

Due to its slow dynamics, the pointing frame can be considered inertial in a first approximation. This implies that, unless external torques are applied, if the body frame changes orientation the momentum will change its distribution in the RWs, but when mapped to the pointing frame it will remain constant and aligned along the α-axis. Therefore, the goal is to generate a torque around α, such that when the attitude is restored, the momentum in the RWs will redistribute itself again, but the one along z will be eventually removed. The solution to this problem involves coupled circular attitude and gimbal trajectories, shifted of 90°. The guidance laws are expressed in (7), imposing clockwise or anticlockwise motions depending on the sign of h_z.

$$\omega = \frac{2\pi}{T} \qquad \begin{aligned} \phi_1 &= \phi_{max}\sin(\omega t)\mathrm{sgn}(h_z) \\ \phi_2 &= \phi_{max}\cos(\omega t) \\ \theta_1 &= -\theta_{max}\cos(\omega t)\mathrm{sgn}(h_z) \\ \theta_2 &= \theta_{max}\sin(\omega t) \end{aligned} \tag{7}$$

From a fixed observer point of view, both the gimbal axis and the z-axis would follow an helicoidal trajectory while the CubeSat proceeds along its track. This strategy has been therefore called Bi-Elicoidal Thruster-Attitude (BETA) trajectory. A visual representation of the sequence is displayed in Fig. 6.

The tunable parameters are the maximum attitude angle ϕ_{max}, the maximum excursion angle θ_{max} and the period of the circular motions T. For the simulations, 5° for the two angles and 20 min for the period have been considered.

3.2 Coasting

The WOL coasting strategies exploit the Solar Array Drive Mechanism (SADM) to tilt differentially the SAs and generate torques on the S/C.

In BepiColombo, these torques are used to counteract the disturbance that arises from the thruster misalignment with respect to the COM. This method is shown to successfully avoid the accumulation of momentum and save RCS propellant with even a few degrees of tilting [12]. The concept of exploiting the SRP for WOL has been investigated for highly elliptical Keplerian orbit [13] and interplanetary travels [14], but in both cases, the solutions presented are coupled with the orbital motion and therefore last several weeks. During normal operations, the SADM is in charge of maintaining the arrays always facing the Sun. The overall tilt angle will be therefore the sum of two contributions, the offset angle $\Delta_{\odot}$ and the relative tilting angle Δ_{rel}, as shown in Fig. 7.

When an attitude motion is imposed, the orientation of the body with respect to the pointing frame can be linked to the attitude angles ϕ_1 and ϕ_2. However, in this case, the two angles will represent the slewing around the δ-axis and α-axis respectively, as displayed in Fig. 8.

3.2.1 SSA & PW Strategies

When the attitude is fixed, it is possible to generate torques only about axes that are perpendicular to β. In particular, two types of effects can be accomplished:

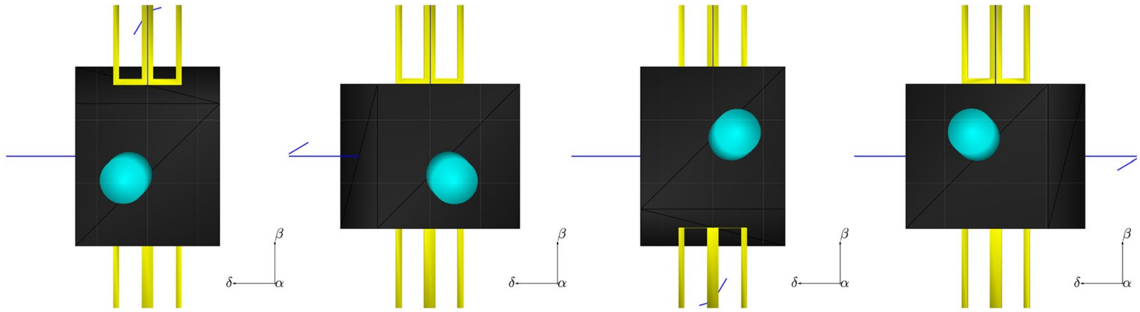

Fig. 6 Sequence of the BETA trajectory along one period

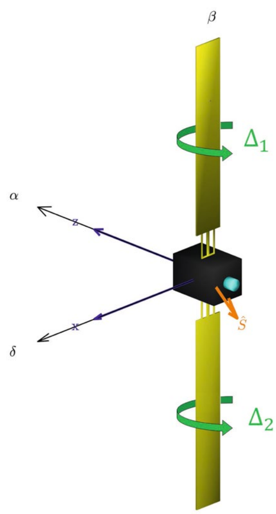

$$\Delta_1 = \Delta_\odot + \Delta_{rel_1} \qquad \Delta_\odot = \arctan\left(\frac{S_\delta}{S_\alpha}\right)$$
$$\Delta_2 = \Delta_\odot + \Delta_{rel_2}$$

Fig. 7 Definition of the SAs tilting angles

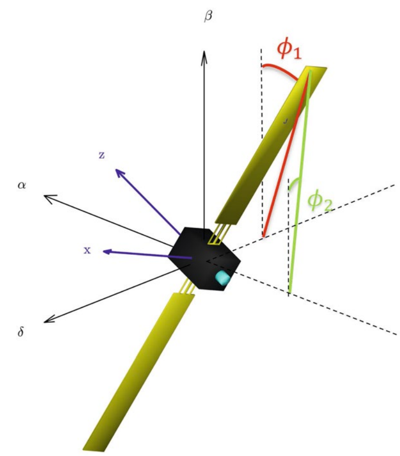

$$A_{b/p} = \begin{bmatrix} \cos\phi_2 & \sin\phi_2 & 0 \\ -\sin\phi_2 & \sqrt{1-(\sin\phi_1)^2-(\sin\phi_2)^2} & -\sin\phi_1 \\ 0 & \sin\phi_1 & \cos\phi_1 \end{bmatrix}$$

Fig. 8 Mapping of the attitude during coasting

- For the Single Solar Array (SSA) strategy, an entire solar wing is kept in shadow such to have a net force on the other one, producing a torque $\boldsymbol{T}_{SSA}$ aligned with $\beta \times \hat{\boldsymbol{S}}$.
- For the PinWheel (PW) strategy, the two wings are tilted one with respect to the other of 70°, just like a pinwheel, producing a torque $\boldsymbol{T}_{PW}$ aligned with $\hat{\boldsymbol{S}}$.

Table 3 Relative tilting angles for SSA & PW strategies

Strategy	SSA_1	SSA_2	PW_1	PW_2
Δ_{rel_1}	0°	90°	−35°	+35°
Δ_{rel_2}	90°	0°	+35°	−35°
$\boldsymbol{T}$	$-\boldsymbol{T}_{SSA}$	$+\boldsymbol{T}_{SSA}$	$-\boldsymbol{T}_{PW}$	$+\boldsymbol{T}_{PW}$

The required combinations of relative tilting angles to accomplish these torques are reported in Table 3. While the choice of 90° in SSA is straightforward, the value of 35° for PW comes from the fact that the SRP torque is the highest at that angle, as it can be seen in Fig. 9.

By selecting the correct combination, both h_x and h_z are guaranteed to approach zero in any situation but not reach it at the same time, since their rate of decrease depends on $\hat{\boldsymbol{S}}$. To solve this issue, a coupling of PW and SSA is employed. Intuitively, this could be a solution since the main difference between the two strategies is that in one case the momentum slopes are of the same sign, in the other case they have opposite signs. This means that after the zero crossing of either h_x or h_z, after a certain time delay Δt the configuration can be changed in such a way to have both of them reach zero at the same time.

The problem is stated in Fig. 10 with an example of a SSA_2 strategy followed by a PW_2.

The time delay can be found re-arranging the equations and applying the final conditions:

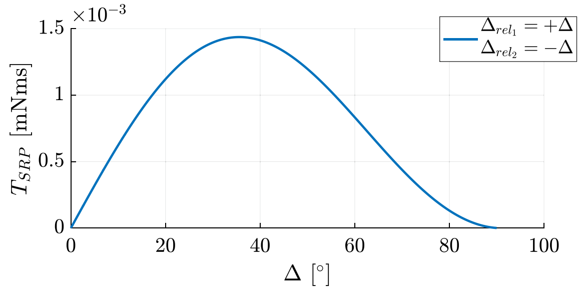

Fig. 9 Torque generated by different relative tilting angles in PW strategy

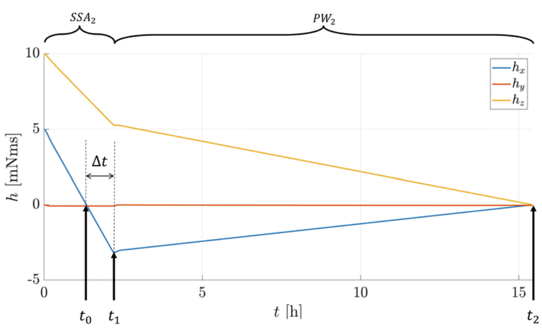

$$\begin{cases} T_{SSA_x} = \dfrac{h_{x_1} - h_{x_0}}{\Delta t} \\ T_{SSA_z} = \dfrac{h_{z_1} - h_{z_0}}{\Delta t} \\ T_{PW_x} = \dfrac{h_{x_2} - h_{x_1}}{t_2 - t_1} \\ T_{PW_z} = \dfrac{h_{z_2} - h_{z_1}}{t_2 - t_1} \end{cases} \quad \begin{array}{ll} \text{find} & \Delta t \\ \text{s.t.} & h_{x_2} = h_{z_2} = 0 \end{array}$$

Fig. 10 Coupling of SSA and PW strategies

$$\Delta t = \frac{h_{x_0} T_{PW_z} - h_{z_0} T_{PW_x}}{T_{SSA_z} T_{PW_x} - T_{SSA_x} T_{PW_z}} \tag{8}$$

The SRP torques for the two configurations are assumed to be estimated on-board prior to the WOL maneuver. In this way, the computer just needs to record the value of the angular momentum that has not crossed zero and apply (8).

3.2.2 SRPW Strategy

Also during coasting, a full WOL can not be completed employing strategies that are based only on a fixed attitude, because there is no possibility to produce torques about the y-axis.

To desaturate this axis, the property of conservation of momentum in a fixed frame can be exploited again. In particular, by coupling a specific SAs trajectory with an attitude motion, torques about the β-axis can be produced, which will eventually dump the momentum on y. The guidance laws are reported in (9). Both trajectories are circular, but the SAs motion is shifted of 90° in amplitude and of $\Delta_{\odot}$ in phase.

$$\begin{aligned} \phi_1 &= \phi_{max} \sin(\omega t) \\ \phi_2 &= \phi_{max} \cos(\omega t) \\ \Delta_{rel_1} &= 90^\circ \min\left(1, 1 + \cos\left(\omega t + \Delta_{\odot}\right)\right) \\ \Delta_{rel_2} &= 90^\circ \min\left(1, 1 - \cos\left(\omega t + \Delta_{\odot}\right)\right) \end{aligned} \tag{9}$$

The two consequences are that the face that should point the Sun is kept close to $\Delta_{rel} = 0°$ for a reasonable fraction of time, and this time slot is consistent with the Sun direction. Moreover, every half period the amplitude of one SA is capped to 90°, i.e. kept in shadow. In this way, the Sun provides a force only to one SA at a time and since this force is always offset from the β-axis on the same "side", a periodic torque about that axis is generated. From an external observer, the CubeSat seems to "wade" against the Solar wind, and therefore this strategy has been called SRP Wading (SRPW). A visual representation is displayed in Fig. 11.

The tunable parameters are again the maximum attitude angle ϕ_{max} and the period of the circular motions T. A good compromise has been found in the simulations using 20° for the former and 2 h for the latter.

3.3 Pyramid Configuration

All the strategies presented so far considered the momentum stored in 3 RWs aligned with the body axes. The case of a pyramid assembly can be treated as well, considering as momentum to dump an *equivalent* momentum, which is the projection of the actual RWs momentum on the body axes. Therefore, the 4 RWs problem is re-written as a 3 RWs case, using the configuration matrix R:

$$\boldsymbol{h}_{eq} = R\, \boldsymbol{h}_{RW} \tag{10}$$

When more than 3 wheels are employed, a *singularity* can occur, in the sense that for specific combinations of the components of $\boldsymbol{h}_{RW}$, the correspondent $\boldsymbol{h}_{eq}$ goes to zero. An example is reported using the configuration matrix of a pyramid assembly oriented along $-x$, such as the one of M-Argo:

$$\boldsymbol{h}_{eq} = \frac{1}{\sqrt{3}} \begin{bmatrix} -1 & -1 & -1 & -1 \\ 1 & -1 & 1 & -1 \\ 1 & 1 & -1 & -1 \end{bmatrix} \begin{bmatrix} k \\ -k \\ -k \\ k \end{bmatrix} = \begin{bmatrix} 0 \\ 0 \\ 0 \end{bmatrix}$$

If such momentum combination occurs, the WOL strategies will fail because the "sensed" momentum will be zero. In this case, the commanded torque should be by-passed and each wheel speed should be decreased directly reducing its rotor spin rate with a proper gain:

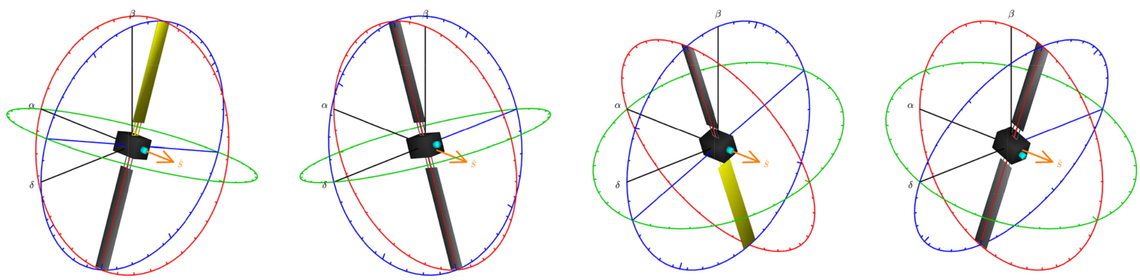

Fig. 11 Sequence of the SRPW trajectory along one period

Fig. 12 State Machine for autonomous WOL

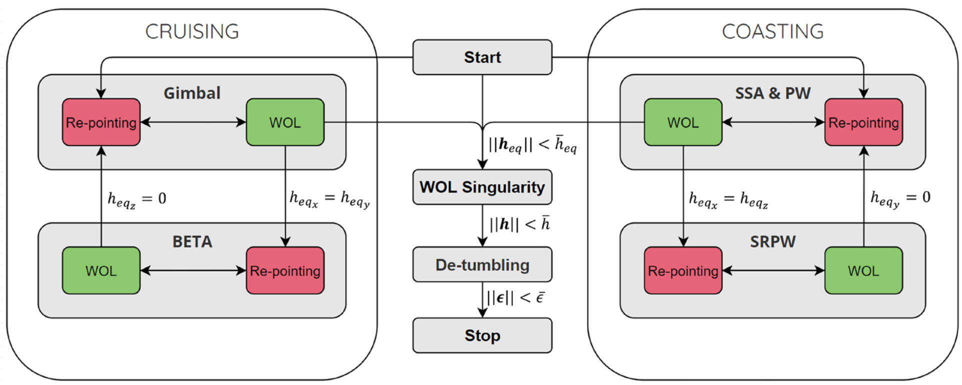

$$\dot{\boldsymbol{h}}_{RW} = -k \ \mathrm{sgn}(\boldsymbol{h}_{RW}) \tag{11}$$

This situation is referred to as WOL Singularity in the context of this work.

3.4 State Machine

To choose the correct strategies and their sequence of application, depending on the angular momentum values and signs, it is convenient to use a State Machine (SM). The architecture depicted in Fig. 12 allows to perform efficiently a full WOL on the entire RW assembly. An exhaustive explanation can be found in [15], but some important aspects that characterize the general decision-making logic should be addressed:

- The first strategy to be used, regardless of being in cruising or coasting, is a fixed-attitude one. This choice allows removing firstly the momentum on "non-singular" axes. In this way, when BETA or SRPW will start, the oscillations on the momentum components will have a mean value of zero.
- The last strategy to be used, regardless of being in cruising or coasting, is a fixed-attitude one. In fact, after completing BETA or SRPW, the reset of the orientation to the pointing frame requires the RWs to store a little amount of momentum, that has to be eventually off-loaded again with fixed-attitude strategies.
- Any strategy state has two inner micro-states. The first one is a re-pointing state and the second one is related to the actual WOL strategy. Any transition to another state is prevented when the current micro-state is re-pointing. This precaution is used to avoid fast and unexpected consecutive transitions between two states.
- The strategies that dump two momentum components at the same time use as exit condition the zero-crossing of the difference between the two components. In this way, there is the assurance that the state will be exited even if the algorithms fail the dumping because one momentum will surely cross the other, sooner or later.

As soon as the sensors measure an equivalent momentum norm lower than a specific threshold, the WOL Singularity state is entered. This state is bypassed in case of a 3 RWs assembly or if the actual momentum norm is also under a specific threshold. A final de-tumbling brings the body frame coincident with the pointing frame before ending the simulation.

4 Simulation Results

The simulations have been performed using WOLAS[1], whose detailed description can be found in [15]. This simulator allows to test the WOL strategies in any type of scenario, but for the sake of brevity only the results for a 4 RWs assembly along the selected activity arc will be now presented. The initial momentum components are chosen randomly, with the constraints of $||\boldsymbol{h}_0|| = 25$ mNms and at least one wheel saturated.

4.1 WOL in Cruising

The results for the cruising scenario simulation are reported in Fig. 13. The momentum is almost completely dumped: after the de-tumbling and final re-pointing the norm is 0.27 mNms, the 0.91% of the initial value. The WOL is accomplished in 3.15 h. In the case of M-Argo, this is equivalent to the 2.2% of the total duration of the cruising arc.

As shown in Fig. 13a, the actual momentum stored in the wheel follows a different trend than the equivalent one. However, in both cases the norm decreases, confirming the fact that the 4 RWs case can be solved as a 3 RWs one. The procedure begins with a Gimbal strategy to remove the momentum on x and y. Then, as soon as h_x crosses h_y, the BETA trajectory begins. As it can be seen in Fig. 13b, the torque generated by the thruster, expressed in the pointing frame, has a non-null component around α-axis, and this is why the momentum accumulated on that quasi-inertial direction can be off-loaded. The torques generated about the other two axes have a much larger magnitude, but their periodic nature does not cause any momentum accumulation on β and δ. However, since h_z crosses zero before the trajectory ends its harmonic period, a final additional Gimbal strategy is required to dump the remaining momentum.

An interesting aspect is the over-thrust required to accomplish such torques. Fig. 13c compare the different thrust levels. The commanded thrust F_{com} is only 0.4% higher than the reference value F_{ref} during the first Gimbal strategy and only 0.7% higher during BETA. These low values of over-thrust, together with the high specific impulse of the thruster, allow saving a relatively high amount of propellant, compared to the case where the RCS is used to obtain the same torques. In particular, the additional consumption with respect to the case without WOL is ≈ 0.002 g using these strategies and ≈ 2 g with a classic RCS desaturation, resulting in mass savings $> 99\%$ when employing the new techniques. Moreover, the higher costs of an engine equipped with a gimbal mechanism is balanced by the fact that the RCS system can be omitted, as outlined in Appendix 1.

An important constraint of the WOL during cruising is to not affect the mission trajectory. During the re-pointing and de-tumbling phases, the thruster is switched off and therefore is not following the reference thrust level. When the WOL is being carried out, on the other hand, it is switched on but is never aligned to the reference pointing vector $\hat{\boldsymbol{\alpha}}$. Thanks to

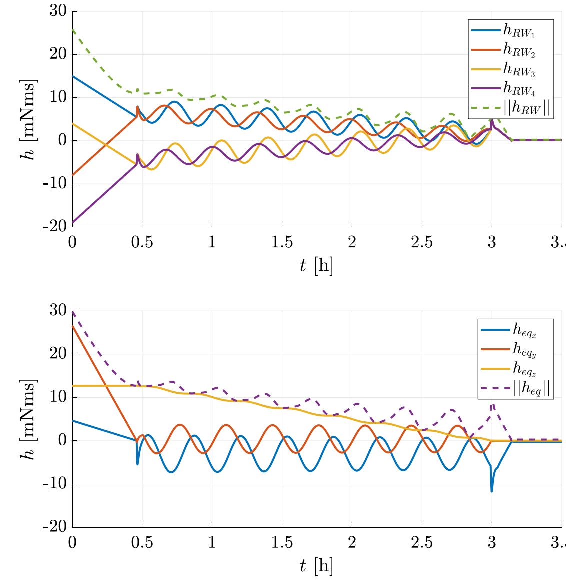

(a) Momentum in RWs and body frame

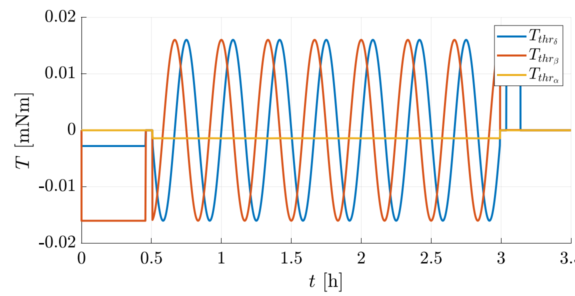

(b) Thruster torque in pointing frame

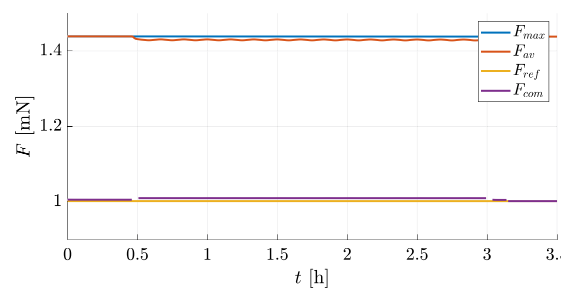

(c) Thrust amplitude

Fig. 13 Results of WOL in a cruising arc

[1] Wheel Off-Loading Astrodynamics Simulator https://gitlab.com/andreapizzetti/wol-simulator.

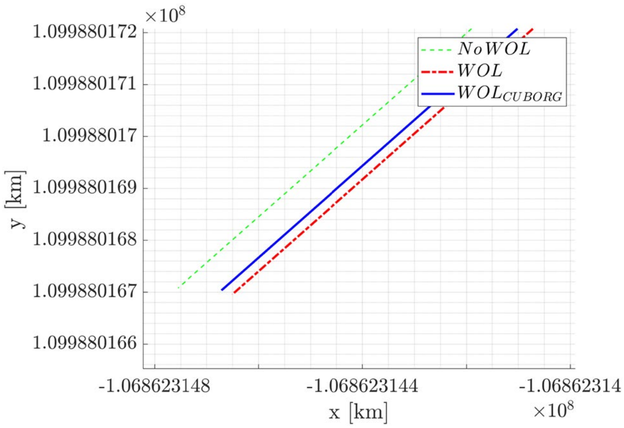

Fig. 14 Trajectory propagation with and without WOL

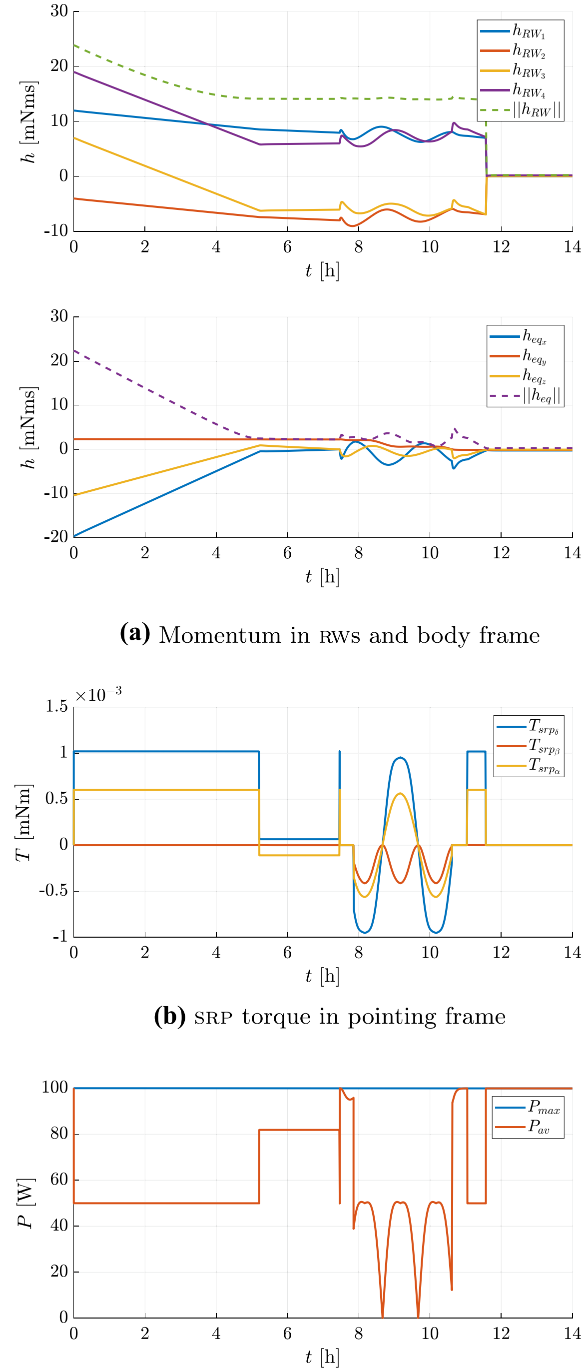

(a) Momentum in RWs and body frame

(b) SRP torque in pointing frame

(c) Power availability

Fig. 15 Results of WOL in a coasting arc

(3), the commanded thrust is augmented to account for this misalignment. The trajectory comparison with respect to the case without WOL is displayed in Fig. 14, together with the same scenario simulated in CUBORG[2], an ephemeris-based high fidelity simulator used for the validation.

The propagation revealed negligible differences of about ≈ 100 m, that in terms of relative error is on the order of $\approx 10^{-7}$. Therefore, the WOL can be performed without any significant risk of deviating from the nominal trajectory.

4.2 WOL in Coasting

The coasting strategies require a much longer time than the cruising ones, due to the lightness of the SRP disturbances. The simulation results for the coasting scenario are reported in Fig. 15. In this case the remaining momentum percentage is about 1.33% and the WOL is completed in more or less 12 h. These strategies would be more constraining in terms of operations for M-Argo since they would last about half the duration of the coasting arc.

Looking at the momentum trends in Fig. 15a, the procedure begins with a SSA strategy, followed by a PW after about 5 h, to remove the momentum on x and z. Then, as soon as h_x crosses h_z, the SRPW strategy is selected to dump the last momentum component. As it can be seen in Fig. 15b, the torque generated by the SAs, expressed in the pointing frame, has oscillatory components on all the axes. However, the component on the β-axis is shifted in magnitude and this results in a net torque effect during the trajectory. The other two components are larger, but they are centered on zero and therefore no momentum is accumulated on δ and α.

In this case, it can be noticed the occurrence of the WOL singularity at about 11.5 h. The equivalent momentum norm $||\boldsymbol{h}_{eq}||$ is practically zero, but the actual momentum $||\boldsymbol{h}_{RW}||$ is still high, about 14 mNms. The spin rate is then forcefully decreased bypassing the commanded torque. This action has the effect to dump the actual momentum stored on the wheel and not produce at the same time an attitude drift because the equivalent torque produced on the platform is zero.

[2] A CUBesat ORbit and GNC tool, DART Group.

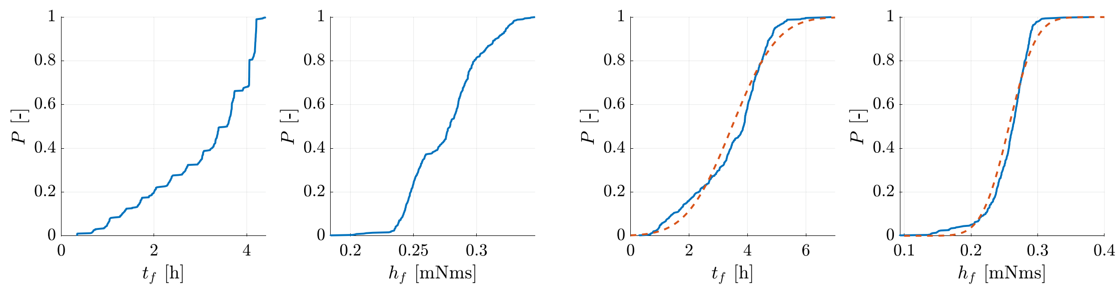

(a) Uncertainty on initial momentum **(b)** Uncertainty on COM displacement

Fig. 16 WOL duration and final momentum norm in case of uncertainties

The main drawback of using such strategies is the decrease in power production. As it can be seen in Fig. 15c, during SSA the power is halved, during PW is around the 80% and in SRPW it oscillates between 0% and 50%. Only during the re-pointing phases, the tilting angles are set to zero and the power produced is equal to the nominal. By carrying out a real-time integration of the power during the simulation, the energy produced is computed to be the 64.5% with respect to the case where no WOL is performed along the same track. This is the price to pay to use these strategies, which are, on the other hand, free of propellant consumption.

As for the cruising strategies, the substitution of the RCS with a SADM is convenient also in terms of costs, as detailed in Appendix 1.

4.3 Sensitivity Analysis

The two main uncertainties to face are the initial angular momentum and the displacement of the COM from the geometric center.

4.3.1 Initial Momentum

A sensitivity analysis has been performed on the cruising scenario with 500 uniformly distributed samples of $\boldsymbol{h}_0$, considering as constraints $||\boldsymbol{h}_0|| = 25$ mNms and at least one wheel saturated. The Empiric Cumulative Distribution Functions (ECDFs) generated from the results are reported in Fig. 16a. In 80% of the cases the WOL is completed in less than 4 h and leaves a residual momentum norm lower than 0.3 mNms.

4.3.2 COM Displacement

The algorithms can be corrected to account for the COM displacement $\boldsymbol{d}_{\odot} = [x_{\odot}\ y_{\odot}\ z_{\odot}]$. The reader is directed to [15] for further explanation on the derivation of the following laws.

The relation in (5) can be re-written with proper approximations into (12).

$$\frac{h_y}{h_x} \approx \frac{T_y}{T_x} = \frac{-x_{\odot} + \left(z_{\odot} - \frac{c}{2}\right)\sin\theta_1}{y_{\odot} - \left(z_{\odot} - \frac{c}{2}\right)\sin\theta_2} \tag{12}$$

Regarding the BETA strategy, the problem can be solved by shifting the gimbal angles trajectory of specific offset angles in such a way to bring $\hat{\boldsymbol{g}}$ nominally aligned with the vector linking the COM with the thruster position. The offset angles to add to (7) are then given by (13).

$$\begin{aligned} \Delta\theta_1 &= \arctan\left(\frac{x_{\odot}}{z_{\odot} + \frac{c}{2}}\right) \\ \Delta\theta_2 &= \arctan\left(\frac{y_{\odot}}{z_{\odot} + \frac{c}{2}}\right) \end{aligned} \tag{13}$$

The sensitivity analysis has been performed with the corrected algorithms considering as constraints $||\boldsymbol{d}_{\odot}|| = 1.2\,\mathrm{cm}$ and again 500 samples. In only 4 cases the WOL took more than 10 h, which means a percentage of success of 99.2%. The results for the successful cases, shown in Fig. 16b, are close to the ones of the previous analysis. In particular, the two data sets can be resembled to Gaussian distributions with a mean WOL duration of about 3.5 h and a mean final angular momentum norm of about 0.26 mNms.

Therefore, if the COM displacement is assumed to be known with a certain degree of accuracy, it is then possible to apply the corrected WOL strategies with minor consequences.

5 Conclusions

The simulations demonstrated the validity of the new techniques in performing the WOL under different deep-space scenarios and initial conditions, in full autonomy. When

Table 4 Quotation ranges for wheel off-loading components in €

Component	RCS
Description	4 electrospray nozzles
Quotation	~250k-350k
Component	**Thruster**
Description	Gridded ion engine
Quotation	~250k
Additional element	2-axis gimbal
Additional cost	~100k-200k
Component	**Solar arrays**
Description	2 wings of 3/4 SPs each
Quotation	~375k-400k
Additional element	Asynchronous SADM
Additional cost	~60k-80k

coming to uncertainties, the algorithms are robust and can still accomplish the goal with mild differences, that in any case do not affect the mission operations nor the trajectory.

All the presented strategies require the use either of a gimbal mechanism or a SADM. Future works should assess their contribution in terms of energy and reaction torques. Moreover, a study on the reliability and endurance of such components would be beneficial, given the presence of moving parts in an harsh environment.

The higher risks that such devices pose are balanced by the fact that the architecture no more needs dedicated momentum-management actuators. This is beneficial from the design viewpoint in terms of mass, volume and cost. The additional propellant that the main thruster should provide for the WOL is a very small percentage of the theoretical one that the RCS requires, due to the former's typical higher specific impulse. In the case of coasting strategies, the mass is completely saved, in exchange for a reduced power production capability.

These advantages, coupled with the possibility to completely automate these techniques, are huge especially when looking at future deep-space CubeSats missions based on miniaturized architectures. It seems that the space industry is becoming more and more biased in favor of this paradigm, and the WOL techniques presented can be considered a promising and effective way to expand both the capabilities and the lifetime of such satellites.

A Market Research

To assess the cost impact of substituting the RCS system functionalities by adding a gimbal mechanism to the thruster or a SADM to the solar arrays, a market research has been carried out. The price quotations for these components are reported in Table 4.

Even considering the worst case prices, the additional cost of a gimbal mechanism would be the 80% of a RCS, for an estimated saving of ~ 50k, while for the SADM this percentage would reduce to the 32%, for an estimated saving of 170k.

Looking at the specific case study application, while few alternatives exist for miniaturized gimballed thrusters, tiltable solar arrays have been recently developed for the CubeSat class. An example is the drive mechanism of Revolv Space[3], capable of providing a pointing accuracy of $\sim 1^\circ$ with a power drawn of ~ 1.5 W.

Funding Open access funding provided by Politecnico di Milano within the CRUI-CARE Agreement.

Data Availability The data that support the findings of this study are available from ESA but restrictions apply to the availability of these data, which were used under license for the current study, and so are not publicly available. Data are however available from the authors upon reasonable request and with permission of ESA.

Declarations

Conflict of interest The authors declare that they have no conflict of interest.

References

1. Schoolcraft, J., Klesh, A., Werne, T.: Marco: Interplanetary mission development on a cubesat scale. In: Space Operations: Contributions from the Global Community, pages 221–231, (2017) https://doi.org/10.1007/978-3-319-51941-8_10
2. Malphrus, B.K., Freeman, A., Staehle, R., Klesh, A.T., Walker, R.: (2021) Interplanetary cubesat missions. In: Cubesat Handbook, pages 85–121. https://doi.org/10.1016/B978-0-12-817884-3.00004-7
3. Stiltner, B.C., Diedrich, B., Becker, C., Bertaska, I., Heaton, A.F., Orphee, J.: Cold gas reaction control system for the near earth

[3] Solar Array Rotary Actuator - SARA https://www.revolvspace.com/product.

asteroid scout cubesat. In: AIAA SPACE and Astronautics Forum and Exposition. https://doi.org/10.2514/6.2017-5185
4. Malphrus, B.K., Brown, K.Z., Garcia, J., et al.: The lunar icecube em-1 mission: Prospecting the moon for water ice. IEEE Aerosp. Electron. Syst. Mag. **34**(4), 6–14 (2019). https://doi.org/10.1109/MAES.2019.2909384
5. Karatekin, Ö., Le Bras, E., Herique, A., Tortora, P., Ritter, B., Scoubeau, M., Moreno, V.M., et al.: Juventas Cubesat for the Hera mision. In: European Planetary Science Congress (2021). https://doi.org/10.5194/epsc2021-750
6. Franzese, V., Topputo, F., Ankersen, F., Walker, R.: Deep-space optical navigation for m-argo mission. J. Astronaut. Sci. (2021). https://doi.org/10.1007/s40295-021-00286-9
7. Topputo, F., Wang, Y., Giordano, C., Franzese, V., Goldberg, H., Perez-Lissi, F., Walker, R.: Envelop of reachable asteroids by m-argo cubesat. Adv. Space Res. **67**(12), 4193–4221 (2021). https://doi.org/10.1016/j.asr.2021.02.031
8. List, M., Bremer, S., Rievers, B., Selig, H.: Modelling of solar radiation pressure effects: parameter analysis for the microscope mission. Int. J. Aerospace Eng. (2015). https://doi.org/10.1155/2015/928206
9. Pidgeon, D., Corey, R., Sauer, B., Day, M.: Two years of on-orbit performance of spt-100 electric propulsion. In: 24th AIAA International Communications Satellite Systems Conference, page 5353, (2006). https://doi.org/10.2514/6.2006-5353
10. Kugelberg, J., Bodin, P., Persson, S., Rathsman, P.: Accommodating electric propulsion on smart-1. Acta Astronaut. **55**(2), 121–130 (2004). https://doi.org/10.1016/j.actaastro.2004.04.003
11. Randolph, T., McElrath, T., Collins, S., Oh, D.: Three-axis electric propulsion attitude control system with a dual-axis gimbaled thruster. In: 47th AIAA/ASME/SAE/ASEE Joint Propulsion Conference & Exhibit, page 5586, (2011). https://doi.org/10.2514/6.2011-5586
12. Kornienko, A., Harris, R.S., Temporelli, P., Ho, K.: Disturbance torque compensation of the bepicolombo spacecraft during interplanetary cruise flight using solar sailing effect. In AIAA Guidance, Navigation, and Control (GNC) Conference, page 5120. https://doi.org/10.2514/6.2013-5120(2013)
13. Mashtakov, Y., Tkachev, S., Ovchinnikov, M.: Use of external torques for desaturation of reaction wheels. J. Guid. Control. Dyn. **41**(8), 1663–1674 (2018). https://doi.org/10.2514/1.G003328
14. Hayashi, N., Ono, G., Shirasawa, Y., Saiki, T., Kawaguchi, J.: Attitude control and angular momentum unloading of spacecraft only with reaction wheels and solar radiation pressure torque. In: The 23rd Workshop on JAXA Astrodynamics and Flight Mechanics, page 75 (2013)
15. Pizzetti, A.: Autonomous wheel off-loading strategies for deep-space cubesats. MSc Thesis, Politecnico di Milano. 1-121 (2021). https://doi.org/10.13140/RG.2.2.13598.00325/1